UC San Diego
UC San Diego Previously Published Works

Title

Multi-wave-mode, multi-frequency detectors for guided wave interrogation of plate structures

Permalink

https://escholarship.org/uc/item/03g51585

Journal

Structural Health Monitoring, 13(2)

ISSN

1475-9217

Authors

Jarmer, Gregory JS
Flynn, Eric B
Todd, Michael D

Publication Date

2014-03-01

DOI

10.1177/1475921713513972

Peer reviewed

Multi-wave-mode, Multi-Frequency Detectors for Guided Wave Interrogation of Plate Structures

Gregory J.S. Jarmer

Department of Structural Engineering, University of California San Diego, 8500 Gilman Drive 0085, La Jolla, CA 92093-0085

Eric Brian Flynn

Los Alamos National Laboratory, Los Alamos NM, 87103

Michael D. Todd

Department of Structural Engineering, University of California San Diego, 8500 Gilman Drive 0085, La Jolla, CA 92093-0085

Abstract:

The detection and localization of damage using an array of closely spaced transducers is investigated theoretically and experimentally using single- and multiple-mode guided wave active sensing models. Detectors are derived using a generalized likelihood ratio approach assuming amplitude, absolute phase, and source location of a scatted wave are unknown, while frequency, group velocity, and phase velocity are known. Theoretical detection performance for processing with each detector is derived and related to the energy-to-noise ratio of a scattered mode as a metric of determining when processing with multiple modes provides increased performance over processing with a single mode. Experimentally, detectors are implemented to detect scattering from a small mass glued to the surface of an aluminum plate with a 7x7 array of transducers. Relative detection and localization performance is compared through receiver operating characteristic curves and histograms of distance from true damage location for 1000 no-damage and damaged measurements. A single-mode, multi-frequency detector is shown to have the best detection and localization performance for the tested damage scenarios.

1. INTRODUCTION

The goal of every structural health monitoring strategy is to effectively detect, locate, and characterize damage to facilitate improved maintenance and performance actions in order to gain life-safety advantage. Common to all strategies is a decision and information extraction process where measurements taken from a structure are processed to determine if damage is or is not present. Ultrasonic guided wave structural health monitoring (UGWSHM) is a specific inspection strategy of longstanding interest due to the ability of guided waves to travel long distances with little attenuation and sensitivity of guided waves to structural defects[1]. Inspection consists of first interrogating the structure with a narrowband input waveform (exciting multiple plate modes) and then analyzing the resulting scattered wave field using a signal processing method (detector) to decide if damage is or is not present. Current guided wave signal processing methods incorporate limited information about the wave propagation environment and rely on the use of a single guided wave mode, typically the first arriving mode, to decide on the presence of damage. Using information from multiple plate modes to detect damage in-service requires knowledge of the wave propagation environment (phase and group velocity) in conjunction with a statistical signal processing technique that properly combines the modes in the presence of inevitable noise or uncertainty.

Detection theory is widely applied in the fields of radar, sonar, and seismology to design statistical signal processing methods that incorporate physical aspects of a problem along with variability due to environmental and operation conditions, in order to decide if an event of interest has occurred[2]. Detection theory is as applied hypothesis testing where the event of interest is stochastically modeled as a composite hypothesis test. The major advantage of resulting processing methods is that associated risks or uncertainty of the problem are incorporated, such as the tradeoff between probability of detection versus false alarm, which is imperative to implementing UGWSHM on in-service structures where directed actions from the decision-making process must be presented with quantified confidence.

1   The majority of UGWSHM signal processing methods are formulated using either engineering

2   intuition, often termed damage-sensitive feature extraction, or through the use of a processing algorithm

3   common in sonar applications[3–9]. Recently several detection theory approaches have been applied to

4   geometrically complex structures via sparse arrays. Enhanced detection of multiple holes in an aluminum

5   plate with stiffeners was achieved by modeling the amplitude of a scattered wave field as Rician

6   distributed due to the large number of secondary reflections caused by the multipath environment. A key

7   feature of this model is that only the envelope of the waveform is used and phase is modeled as unknown

8   due to the sparsity of the array. Damage in the form of a loose bolted connection in a frame structure and

9   cracks/holes in a fuselage rib were detected using an energy detector resulting from modeling the

10   reverberated wave field as Rayleigh distributed, which results when minimal information about the

11   structure's wave propagation is known[11].

12   This study seeks to detect and locate scattering from a single damage source using a dense array

13   of sensing points, a single off-array actuator, and a generalized multi-wave-mode scattering model. A

14   binary composite hypothesis model is formulated, where the null hypothesis is that no damage-induced

15   scattering is present, and the alternative hypothesis is that damaged-induced scattering is present from

16   multiple waves with different wavenumbers. Amplitude, absolute phase, and scattering location (range

17   and bearing) are assumed unknown while temporal frequency, spatial frequency (wavenumber), and

18   group velocity are assumed known. Detectors are derived using a generalized likelihood ratio test

19   approach and theoretical detection performance presented. Experimentally, the detector is implemented

20   for an aluminum plate with damage represented as a glued surface mass (Figure 1). Detector performance

21   for processing assuming a single wave-mode vs. multiple wave-modes is compared using receiver

22   operator characteristic (ROC) curves for 1000 experimental runs. Additionally, the ability of the detector

23   to properly locate the mass is presented via histograms of the distance between actual and estimated

24   location.

25   The main contributions of this paper to the UGWSHM field are: (1) The derivation of a general

26   dense array detector that incorporates scattering from multiple wave-modes with different wavenumbers,

1   (2) A theoretical derivation of detection performance that predicts when it is beneficial to process data

2   using either a single scattered wave-mode or multiple scattered wave-modes, and (3) Experimental

3   validation of the resulting detectors through a large number of experimental trials, enabling a statistical

4   comparison of performance.

5   The organization of the paper is as follows: The problem statement and assumptions made

6   concerning the wave propagation environment are first outlined followed by the formulation of a general

7   multi-mode scattering model. Four specific signal models applicable to UGWSHM are then formulated:

8   (1) single A_0 mode scattering, (2) single S_0 mode scattering, (3) $A_0 + S_0$ mode scattering, and (4) multi-

9   frequency A_0 mode scattering. Detectors for each signal model are then derived using a generalized

10   likelihood ratio approach in addition to theoretical detection performance. Experimental implementation

11   follows, and the limitations and model assumptions are discussed.
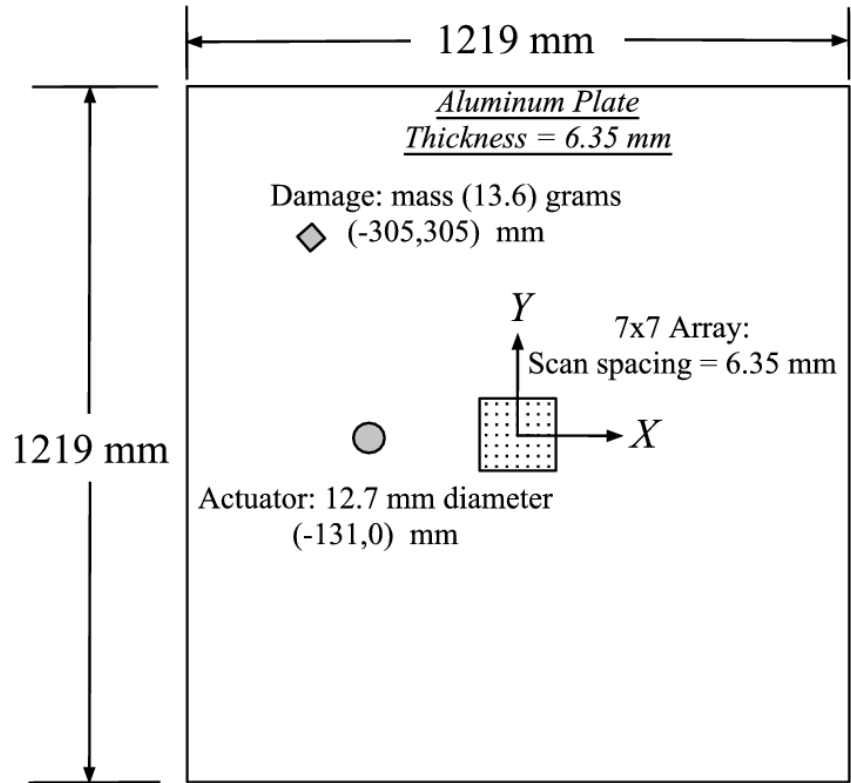
12

13   Figure 1 Experimental layout: Actuator is a piezoelectric disc while array is sensed via a scanning laser Doppler vibrometer.

4

1 2. SIGNAL MODEL

2   The active sensing scheme illustrated in Figure 1 is assumed where a surface mounted piezoelectric

3   transducer excited by a modulated tone burst, applies both in-plane and out of plane surface strains,

4   inducing P narrowband guided wave modes[12]. The induced guided wave modes are characterized as

5   either anti-symmetric or symmetric depending upon their associated strain/displacement profile relative to

6   the mid-plane of the plate. An array of M sensing points located at arbitrary position $\mathbf{p}_m = \begin{bmatrix} p_{x_m} & p_{y_m} \end{bmatrix}^T$,

7      $m=0\dots M\text{-}1$, samples the spatiotemporal field for backward or forward scattering from damage with inter-

8   element transducer spacing made sufficiently small to allow phase-coherent processing and to avoid

9   effects from spatial aliasing[13]. The scattering source is assumed to be located at least several wavelengths

10   away from the array center, and any scattering received by the array can be approximated as a plane wave

11   with wavevector, $\mathbf{k}^{\{\alpha\}}$, where the superscript $\alpha = 1\dots P$, represents the scattered wave mode. Figure 2,

12   illustrates a received scattering field for $P = 2$.
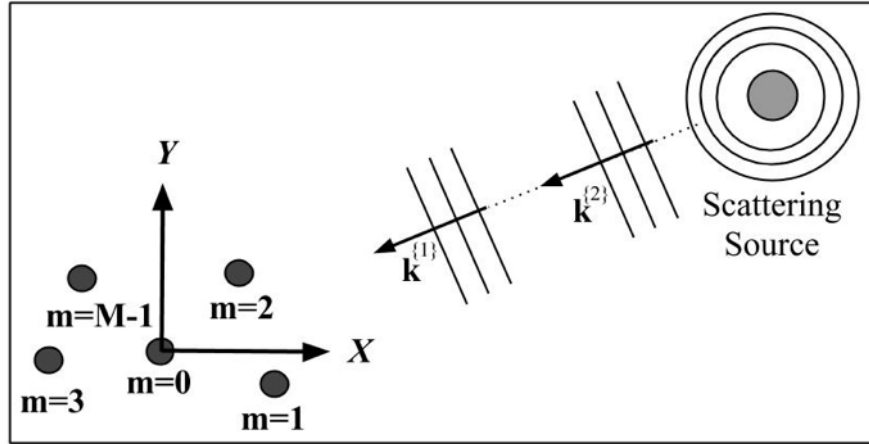
14   Figure 2 Assumed active sensing signal model for scattering source in the far field.

15   A scattered signal received at the mth sensing point and sampled discretely in time is mathematically

16   modeled as

17
$$\tilde{s}_m[n] = \sum_{\alpha=1}^{P} A^{\{\alpha\}} \exp\left[\phi^{\{\alpha\}}\right] \Pi^{\{\alpha\}}[n,r] \exp\left[j2\pi f^{\{\alpha\}} n\right] \exp\left[-j2\pi f^{\{\alpha\}} \tau_m^{\{\alpha\}}\right],$$
(1)

1   where $A^{\{\alpha\}}$ is amplitude, $\phi^{\{\alpha\}}$ is absolute phase relative to the scattering source, $f^{\{\alpha\}}$ is the temporal

2   frequency in cycles/sample, and $\tau_m^{\{\alpha\}}$ is the relative inter-element phase delay in samples due to the

3   direction of propagation for a given wavevector[2,13]. The discrete time signal $\tilde{s}_m[n]$ is obtained by

4   sampling a continuous time signal $\tilde{s}_m(t)$ at $t = n\Delta$, mathematically represented as $\tilde{s}_m[n] = \tilde{s}_m[n\Delta]$.

5   Here, Δ is the sampling period with units of sec/sample. In a similar manner, the continuous temporal

6   frequency with units of cycles/sec transforms to units of cycles/sample after sampling. In practice, a

7   complex signal is obtained through the analytic signal representation of sampled data. An observation is

8   composed of N samples ranging from $n = 0 \ldots N - 1$. The inter-element phase delay, referenced at the array

9   center for a wave with mode α propagating in direction β, is

$$\tau_m^{\{\alpha\}} = -\frac{\mathbf{p}_m^T}{c_p^{\{\alpha\}}\Delta}\begin{bmatrix} \cos(\beta) & \sin(\beta) \end{bmatrix}^T,$$

10 (2)

11   where $c_p^{\{\alpha\}}$ is the phase velocity. The function $\Pi^{\{\alpha\}}[n,r]$ is the boxcar function that represents the time

12   window when wave mode α, scattered from a source a distance r away, is present at all array transducers,

$$\Pi^{\{\alpha\}}[n,r] = H\left[n - n^{\{\alpha\}}\right] - H\left[n - \left(n^{\{\alpha\}} + K^{\{\alpha\}}\right)\right],$$

13 (3)

14   where $n^{\{\alpha\}} = r/\left(c_g^{\{\alpha\}}\Delta\right)$ is the arrival sample, $c_g^{\{\alpha\}}$ is group velocity, H is the Heaviside function, and

15   $K^{\{\alpha\}}$ is the length of the time window. Figure 3 illustrates an example single sensor observation

16   according to the sensing model described in Equation (1) for $P = 2$. A Heaviside window is chosen for

17   mathematical simplicity of the resulting equations. In reality the envelope of a guided wave signal tapers

18   smoothly at the edges and has unique bandwidth and side lobe structure in the frequency domain. If the

19   bandwidths of the corresponding guided waves are known a priori then a corresponding window function

1   other than a Heaviside function could be used. The boxcar window serves to segment in time when an

2   individual wave-mode is present at all array sensors.

3   This signal model is applicable to direct scattering from damage and does not account for

4   reflections from geometric features such a plate edges. Reflections from geometric features are negated

5   by subtracting a baseline measurement state, often termed baseline subtraction, from a unknown damaged

6   measurement state resulting in a signal that only contains scattering from damage[14]. A baseline

7   subtraction approach is used in this study for all experimental work.
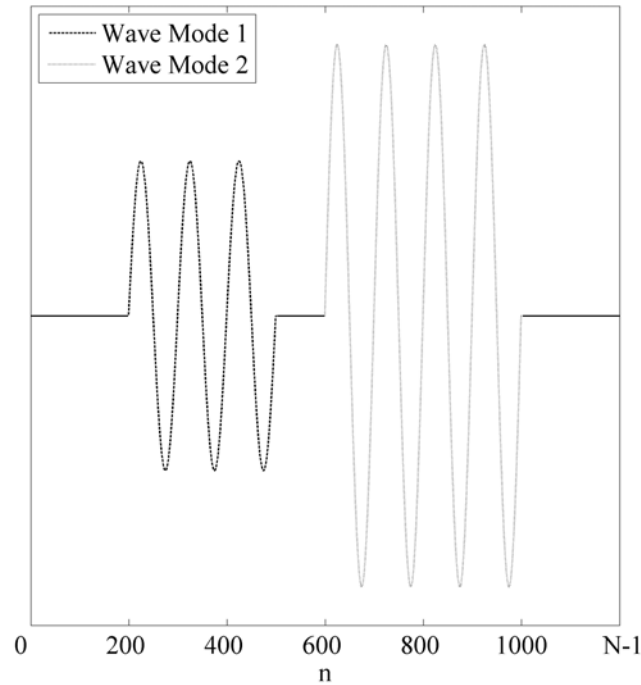

8

9   Figure 3 Single sensor observations for two signals not overlapping in time.

10   2.1   Single, multi-modal and multi-frequency signal model

11   UGWSHM with a dense array in practice is predominately limited to inspection frequencies below

12   300 kHz and $P = 2$ modes, due to the spatial Nyquist sampling criteria set by the inter-element array

13   spacing and dispersion relation of the material. For aerospace structures with weight constraints, this

14   involves inspection of fuselage and structural members with thicknesses up to tens of millimeters. An

1   example case is inspecting a 6.35 mm thick aluminum plate with an inter-element array spacing of 6.35

2   mm. The largest wavenumber before spatial aliasing occurs is $\simeq 78$ m^{-1} corresponding to a frequency of

3   180 kHz for the A_0 mode (Figure 4).
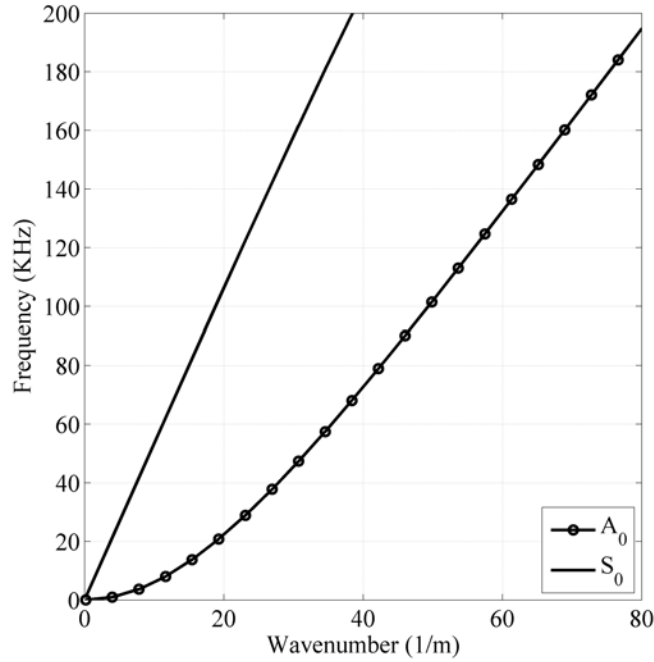
4

5   Figure 4 Frequency-wavenumber curves for an aluminum plate of 6.35 mm thickness.

6   Assuming that both A_0 and S_0 modes are induced at a single actuation frequency, the scattered

7   waves received by the array are of form: $\left(A_0 \rightarrow A_0 \right) + \left(S_0 \rightarrow S_0 \right)$, $\left(A_0 \rightarrow S_0 \right) + \left(S_0 \rightarrow S_0 \right)$,

8    $\left(A_0 \rightarrow A_0 \right) + \left(S_0 \rightarrow A_0 \right), \left(A_0 \rightarrow S_0 \right) + \left(S_0 \rightarrow A_0 \right)$, where the notation $\left(A_0 \rightarrow A_0 \right)$ represents an induced A_0

9   mode scattering off of damage and arriving at the array as an A_0 mode, whereas $\left(A_0 \rightarrow S_0 \right)$ represents an

10   A_0 to S_0 mode conversion at the damage[15]. Similarly, $\left(S_0 \rightarrow S_0 \right)$ represents an induced S_0 mode scattering

11   off of damage and arriving as an S_0 mode, and $\left(S_0 \rightarrow A_0 \right)$ represents an S_0 to A_0 mode conversion at the

12   damage. Combining bracketed terms with a "+" sign simply implies the presence of multiple scattered

13   mode combinations detected by the array. As an example of two incident modes without conversion, e.g.,

1    $\left(A_0 \rightarrow A_0\right)+\left(S_0 \rightarrow S_0\right)$ and letting $\alpha = A_0, S_0$ for $f^{\{A_0\}} = f^{\{S_0\}} = f$ in Equation (1), the resulting multi-

2   modal signal model is

$$
\begin{aligned}
\tilde{s}_m[n] &= A^{A_0} \exp\left[\phi^{A_0}\right]\Pi^{A_0}[n,r]\exp\left[j2\pi fn\right]\exp\left[-j2\pi f\tau_m^{A_0}\right]+ \\
&\quad A^{S_0} \exp\left[\phi^{S_0}\right]\Pi^{S_0}[n,r]\exp\left[j2\pi fn\right]\exp\left[-j2\pi f\tau_m^{S_0}\right] \quad . \\
&= A_0^{\{f\}} + S_0^{\{f\}}
\end{aligned}
\tag{4}
$$

4   For all the various mode conversion possibilities, Equation (4) takes the same form except that $\Pi^{A_0}[n,r]$

5   terms are replaced by $\Pi^{A_0 \rightarrow S_0}[n,r]$, representing the different arrival time of an outgoing A_0 mode and a

6   scattered S_0 mode. Similarly, a single-mode model is obtained by letting $P = 1$ in Equation (1). For the

7   case of $\left(A_0 \rightarrow A_0\right)$ the resulting single-mode model is

$$
\tilde{s}_m[n] = A^{A_0} \exp\left[\phi^{A_0}\right]\Pi^{A_0}[n,r]\exp\left[j2\pi fn\right]\exp\left[-j2\pi f\tau_m^{A_0}\right] = A_0^{\{f\}}.
\tag{5}
$$

9   Equation (1) is thus a generalized model allowing modeling of the many damage scattering situations

10   encountered in UGWSHM where only a single damage source is present. Even multiple actuation

11   frequencies are accommodated by letting $f^{\{1\}} \neq f^{\{2\}}$ in Equation (1); using an $\left(A_0 \rightarrow A_0\right)$ case for

12   illustration, the scattering at two different actuation frequencies is

$$
\begin{aligned}
\tilde{s}_m[n] &= A^{A_0,f1} \exp\left[\phi^{A_0,f1}\right]\Pi^{A_0,f1}[n,r]\exp\left[j2\pi f^{A_0,f1}n\right]\exp\left[-j2\pi f^{A_0,f1}\tau_m^{A_0,f1}\right]+ \\
&\quad A^{A_0,f2} \exp\left[\phi^{A_0,f2}\right]\Pi^{A_0,f2}[n,r]\exp\left[j2\pi f^{A_0,f2}n\right]\exp\left[-j2\pi f^{A_0,f2}\tau_m^{A_0,f2}\right] \quad . \\
&= A_0^{\{f_1\}} + A_0^{\{f_2\}}
\end{aligned}
\tag{6}
$$

14

15

16

1   3. DETECTOR DERIVATION

2   It is assumed that amplitude, absolute phase, and scattering location for the signal model examples in

3   Equations (4)-(6) are deterministic but unknown and that the excitation frequency, phase velocity, and

4   group velocity are known. This represents an UGWSHM active sensing scheme where a known actuation

5   signal interrogates a plate structure of known dispersion relation for damage of unknown size and

6   location. Determining the presence of damage is equivalent to a binary composite hypothesis test where

7   under the null hypothesis, H_0, only noise is present and under the alternative hypothesis, H_1, noise and

8   scattering from damage are present.

9   Noise is assumed to be Gaussian distributed with zero mean and known variance. In practice, the

10   noise environment for UGWSHM inspection of complicated structures results in a highly correlated

11   noise/interference field that is non-Gaussian and non-stationary due to the multipath environment and

12   variations in operating conditions. However, when an ideal signal baseline subtraction is used, the

13   resulting signal contains only Gaussian noise under H_0 and Gaussian noise plus a damage scattered

14   signal under H_1[14,16]. Thus, the models assumed in Equations (4)-(6), consisting of a single scattering

15   source, are suited only to structures where reflections from boundaries are minimized via baseline

16   subtraction. Non-ideal baseline subtraction and secondary scattering, e.g., waves that first scatter off of

17   damage and then interact with a boundary resulting in damage appearing to originate from a boundary,

18   are a major source of error in UGWSHM inspection[10,17]. To account for a non-Gaussian and non-ideal

19   baseline subtraction conditions requires modeling of interfering boundary reflections and is not studied in

20   this investigation.

21   The observed array data under each hypothesis is a vector random variable and described by a

22   probability density function (PDF). Letting $\tilde{\mathbf{x}}$ represent the observed array data vector, the PDF under

23   H_0 is represented as $p(\tilde{\mathbf{x}}; H_0)$ and under H_1 as $p(\tilde{\mathbf{x}}; \boldsymbol{\theta}_1, H_1)$, where $\boldsymbol{\theta}_1$ is a vector of the unknown

1   parameters. A generalized likelihood ratio test (GLRT) is used to decide between the two hypotheses. The

2   GLRT decides H_1 if

$$L_G\left(\tilde{\mathbf{x}}\right) = \frac{p\left(\tilde{\mathbf{x}};\hat{\boldsymbol{\theta}}_1, H_1\right)}{p\left(\tilde{\mathbf{x}};H_0\right)} > \gamma,$$ (7)

4   where $\hat{\boldsymbol{\theta}}_1$ is the maximum likelihood estimate (MLE) of $\boldsymbol{\theta}_1$ under H_1, i.e., the value of $\boldsymbol{\theta}_1$ that maximizes

5    $p\left(\tilde{\mathbf{x}};\boldsymbol{\theta}_1, H_1\right)$[18].

6   ### 3.1   Multi-modal array detector

7   To formulate the GLRT test, the classical linear model for complex data is used[2,18], where first it is

8   assumed that the only unknown parameters are amplitude and phase and that any noise present is

9   distributed according to a complex white Gaussian PDF with zero mean and known variance σ^2,

10   represented as $\tilde{\mathbf{w}} \sim CN\left(0,\sigma^2\right)$. Writing Equation (4) in vector format, the detection problem is

11   represented formally as

$$\begin{aligned} H_0: \quad &\tilde{\mathbf{x}}[n] = \tilde{\mathbf{w}}[n] & n = 0,1,...,N-1 \\ H_1: \quad &\tilde{\mathbf{x}}[n] = \tilde{\mathbf{w}}[n] + \tilde{\mathbf{s}}[n] & n = 0,1,...,N-1 \end{aligned},$$ (8)

13   where

$$\tilde{\mathbf{x}}[n] = \begin{bmatrix} \tilde{x}_0[n] \\ \tilde{x}_1[n] \\ \vdots \\ \tilde{x}_{M-1}[n] \end{bmatrix},$$ (9)

15   and

$$
1 \qquad \tilde{\mathbf{s}}[n]=\begin{bmatrix}\tilde{s}_0[n]\\ \tilde{s}_1[n]\\ \vdots\\ \tilde{s}_{M-1}[n]\end{bmatrix}=\begin{bmatrix}\Pi^{A_0}[n,r]\exp\left[j2\pi f\left(n-\tau_0^{A_0}\right)\right] & \Pi^{S_0}[n,r]\exp\left[j2\pi f\left(n-\tau_0^{S_0}\right)\right]\\ \Pi^{A_0}[n,r]\exp\left[j2\pi f\left(n-\tau_1^{A_0}\right)\right] & \Pi^{S_0}[n,r]\exp\left[j2\pi f\left(n-\tau_1^{S_0}\right)\right]\\ \vdots & \vdots\\ \Pi^{A_0}[n,r]\exp\left[j2\pi f\left(n-\tau_{M-1}^{A_0}\right)\right] & \Pi^{S_0}[n,r]\exp\left[j2\pi f\left(n-\tau_{M-1}^{S_0}\right)\right]\end{bmatrix}\begin{bmatrix}A^{A_0}\exp\left[j\phi^{A_0}\right]\\ A^{S_0}\exp\left[j\phi^{S_0}\right]\end{bmatrix}. \qquad (10)
$$

2   The vector $\tilde{\mathbf{s}}[n]$ is of dimension $M\times 1$ and is referred to as an array snapshot since it captures a wave

3   propagating through the array at a single time sample. Arranging the array snapshots in one large vector

4   results in

$$
5 \qquad \tilde{\mathbf{s}}=\begin{bmatrix}\tilde{\mathbf{s}}[0]\\ \tilde{\mathbf{s}}[1]\\ \vdots\\ \tilde{\mathbf{s}}[N-1]\end{bmatrix}=\begin{bmatrix}\mathbf{h}_1[0] & \mathbf{h}_2[0]\\ \mathbf{h}_1[1] & \mathbf{h}_2[1]\\ \vdots & \vdots\\ \mathbf{h}_1[N-1] & \mathbf{h}_2[N-1]\end{bmatrix}\begin{bmatrix}A^{A_0}\exp\left[j\phi^{A_0}\right]\\ A^{S_0}\exp\left[j\phi^{S_0}\right]\end{bmatrix}=\begin{bmatrix}\mathbf{h}_1 & \mathbf{h}_2\end{bmatrix}\begin{bmatrix}A^{A_0}\exp\left[j\phi^{A_0}\right]\\ A^{S_0}\exp\left[j\phi^{S_0}\right]\end{bmatrix}=\mathbf{H}\boldsymbol{\theta}_1, \qquad (11)
$$

6   where $\mathbf{H}$ is termed the observation matrix and is of size $MN\times 2$, and $\boldsymbol{\theta}_1$ is a 2×1 vector of unknown

7   parameters. Note that Equation (11) represents the concatenation of all time instances of $\mathbf{h}_1[n]$ for the

8   A_0 mode and similarly of $\mathbf{h}_2[n]$ for the S_0 mode. The GLRT decides H_1 if

$$
9 \qquad T(\tilde{\mathbf{x}})=\frac{\hat{\boldsymbol{\theta}}_1^H\mathbf{H}^H\mathbf{H}\hat{\boldsymbol{\theta}}_1}{\sigma^2/2}>\gamma', \qquad (12)
$$

10   where $\hat{\boldsymbol{\theta}}_1$ is

$$
11 \qquad \hat{\boldsymbol{\theta}}_1=\left(\mathbf{H}^H\mathbf{H}\right)^{-1}\mathbf{H}^H\tilde{\mathbf{x}}. \qquad (13)
$$

12   Substitution of Equations (11) and (13) into (12) and simplifying results in

$$
13 \qquad T(\tilde{\mathbf{x}})=\frac{2}{\sigma^2\left((KM)^2-\mathbf{h}_1^H\mathbf{h}_2\mathbf{h}_2^H\mathbf{h}_1\right)}\left[\left|\mathbf{h}_1^H\tilde{\mathbf{x}}\right|^2+\left|\mathbf{h}_2^H\tilde{\mathbf{x}}\right|^2-2\operatorname{Re}\left[\tilde{\mathbf{x}}^H\mathbf{h}_1\mathbf{h}_1^H\mathbf{h}_2\mathbf{h}_2^H\tilde{\mathbf{x}}\right]\right]. \qquad (14)
$$

1   The detector from Equation (14) is composed of three terms. The first two terms are inner products

2   between the signal vectors and the data vector while the third term is a multiplication of the same inner

3   products along with an inner product between the signal vectors. Rewriting the first term in non-vector

4   notation gives

$$\left|\mathbf{h}_1^H\tilde{\mathbf{x}}\right|^2 = \left|\sum_{m=0}^{M-1}\sum_{n=0}^{N-1}\tilde{x}_m[n]\Pi^{A_0}[n,r]\exp\left[-j2\pi f\left(n-\tau_m^{A_0}\right)\right]\right|^2. \tag{15}$$

6   Changing the order of summation and incorporating the boxcar function allows Equation (15) to be

7   written as

$$\left|\mathbf{h}_1^H\tilde{\mathbf{x}}\right|^2 = \left|\sum_{n=0}^{N-1}\tilde{x}_B[n]\exp\left[-j2\pi fn\right]\right|^2, \tag{16}$$

9   where

$$\tilde{x}_B[n] = \sum_{m=0}^{M-1}\tilde{x}_m[n]\exp\left[j2\pi f\tau_m^{A_0}\right]. \tag{17}$$

11   In this form, Equation (16) is recognized as a periodogram at known frequency f, and Equation (17) is a

12   phased array beam former for the A_0 mode. The same processing results for the second term of Equation

13   (14), except that the beam forming operation is for the S_0 mode. The third term contains the product

14   between the discrete Fourier transform of each beam formed mode with the inner product between the

15   first and second signals,

$$\mathbf{h}_1^H\mathbf{h}_2 = \sum_{m=0}^{M-1}\sum_{n=0}^{N-1}\Pi^{A_0}[n,r]\exp\left[-j2\pi f\left(n-\tau_m^{A_0}\right)\right]\Pi^{S_0}[n,r]\exp\left[j2\pi f\left(n-\tau_m^{S_0}\right)\right]. \tag{18}$$

17   The first thing to notice is that $\mathbf{h}_1$ and $\mathbf{h}_2$ are orthogonal, $\mathbf{h}_1^H\mathbf{h}_2 = 0$, if they are completely separated in

18   time due to a difference in group velocities and a damage source located sufficiently far away (Figure 3).

13

1 Separation in arrival time occurs for wave-modes at the same temporal frequency, i.e. A_0 and S_0 both at

2 temporal frequency f, and for an individual wave-mode at different temporal frequencies, i.e. A_0 at

3 temporal frequency $f^{\{1\}}$ and $f^{\{2\}}$. Additionally, orthogonally also occurs in frequency and wavenumber,

4 dependent upon the relative separation in wavenumber and or frequency, similar in concept to spectral

5 leakage in conventional discrete Fourier analysis[13,19].

6   The detector from Equation (14) beam forms for each mode present, combines the estimated

7 power of each mode at a known frequency, and subtracts any correlation between the modes. When $\mathbf{h}_1$

8 and $\mathbf{h}_2$ are orthogonal, Equation (14) simplifies to

$$T(\tilde{\mathbf{x}}) = \frac{2}{\sigma^2 \left((KM)^2 \right)} \left[\left| \mathbf{h}_1^H \tilde{\mathbf{x}} \right|^2 + \left| \mathbf{h}_2^H \tilde{\mathbf{x}} \right|^2 \right]. \tag{19}$$

10 Equation (19) assumes that the only unknown parameters are amplitude and phase. In practice the

11 location of the damage source is unknown, resulting in arrival time and angle unknown. To estimate these

12 parameters, Equation (19) is numerically maximized over all possible range and bearing combinations

13 represented as,

$$T(\tilde{\mathbf{x}}) = \max_{r,\beta} \frac{2}{\sigma^2 \left((KM)^2 \right)} \left[\left| \mathbf{h}_1^H \tilde{\mathbf{x}} \right|^2 + \left| \mathbf{h}_2^H \tilde{\mathbf{x}} \right|^2 \right]. \tag{20}$$

15 This is possible since the PDF under H_0 is nonnegative and does not depend upon on r or β. Similarly,

16 the detector under only a single propagating mode model is found by setting $\mathbf{h}_2 = 0$ in Equation (20),

$$T(\tilde{\mathbf{x}}) = \max_{r,\beta} \frac{2}{\sigma^2 \left((KM)^2 \right)} \left[\left| \mathbf{h}_1^H \tilde{\mathbf{x}} \right|^2 \right]. \tag{21}$$

18 3.2   Multi-frequency array detector

1   The multi-frequency signal model from Equation (6) results in a detector of the same form as

2   Equation (14). Orthogonally between $\mathbf{h}_1$ and $\mathbf{h}_2$ again results in Equation (20) except now the detector

3   has components of the form

4
$$\left|\mathbf{h}_\alpha^H \tilde{\mathbf{x}}\right|^2 = \left|\sum_{m=0}^{M-1}\sum_{n=0}^{N-1} \tilde{x}_m\left[n\right]\Pi^{A_0,f_\alpha}\left[n,r\right]\exp\left[-j2\pi f^{\{A_0,f_\alpha\}}\left(n-\tau_m^{A_0,f_\alpha}\right)\right]\right|^2. \tag{22}$$

5   The detector again beam forms for each signal then computes a periodogram.

6   4. DETECTOR PERFORMANCE

7   The probability of false alarm and detection for the GLRT of Equation (12) is

8
$$P_{FA} = Q_{\chi_4^2}\left(\gamma'\right), P_D = Q_{\chi_4^2(\lambda)}\left(\gamma'\right). \tag{23}$$

9    $Q_{\chi_4^2}$ is the right tail probability for a central Chi-Squared PDF with 4 degrees of freedom and similarly

10   $Q_{\chi_4^2(\lambda)}$ is the right tail probability for a non-central Chi-Squared PDF with 4 degrees of freedom and non-

11   centrality parameter λ equal to,

12
$$\lambda = \frac{\boldsymbol{\theta}_1^H \mathbf{H}^H \mathbf{H} \boldsymbol{\theta}_1}{\sigma^2/2} = \text{ENR first mode} + \text{ENR second mode}. \tag{24}$$

13   Central and non-central Chi-Squared PDFs result since the detector sums the square of complex Gaussian

14   random variables. The non-centrality parameter is the energy to noise ratio (ENR) of the assumed model.

15   An example of the non-centrality parameter for the multi-mode detector from Equation (24) is

16
$$\text{ENR first mode} + \text{ENR second mode} = \frac{KM\left(A^{A_0}\right)^2}{\sigma^2/2} + \frac{KM\left(A^{S_0}\right)^2}{\sigma^2/2}. \tag{25}$$

1   Similar forms result for the multi-frequency detector. Scanning over $L = r \times \beta$ independent range-bearing

2   combinations in Equation (20) results in a probability of false alarm of

$$P_{FA} = 1 - \left(1 - \exp\left(-\frac{\gamma'}{2}\right)\left(1 + \frac{\gamma'}{2}\right)\right)^L. \tag{26}$$

4   This contrasts to the probability of false alarm and detection for a single mode where the number of

5   degrees of freedom is reduced to two, resulting in

$$P_{FA} = 1 - \left(1 - \exp\left(-\frac{\gamma'}{2}\right)\right)^L, \tag{27}$$

7   and non-centrality parameter

$$\lambda = \text{ENR first mode} = \frac{KM\left(\left(A^{A_0}\right)^2\right)}{\sigma^2 / 2}. \tag{28}$$

9   Since the number of degrees of freedom and the ENRs are different for single- and multiple-mode

10   models, it is unclear if processing via a single mode results in better detection performance than

11   processing via multiple modes. To investigate this, the probability of detection for both models is

12   numerically determined by varying the ENR of the first mode for fixed ENR values of the second mode,

13   while holding the probability of false alarm and L constant. Figure 5, compares the resulting output for

14   second mode ENR values of -5, 0 and 10 dB, probability of false alarm of 10^{-2} and $L = 48 \times 360$. Here

15   dB is calculated as $10\log_{10}(\text{ENR})$. Three cases result: (1) A second mode ENR of 10 dB results in

16   increased performance, (2) A second mode ENR of -5 dB results in decreased performance, and (3) A

17   second mode ENR of 0 dB results in a mixed performance with the transition occurring at a first mode

18   ENR of 5 dB. The transition value is the point where processing with both modes becomes beneficial.
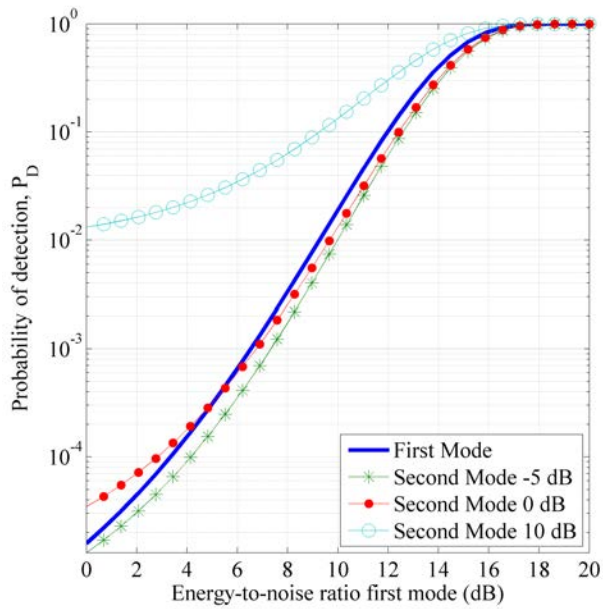
1

2
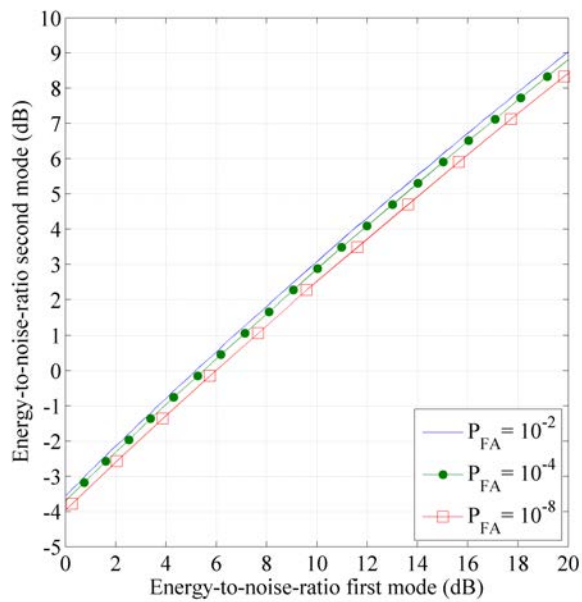Figure 5 Probability of detection vs. ENR for single and multimode processing.

3 Figure 6 is a plot of transition values for varying first and second mode ENR values at fixed probability of

4 false alarm values of $10^{-2}, 10^{-4}$ and 10^{-8}, $L = 48 \times 360$. Choosing a second mode value of 0 dB and false

5 alarm curve of 10^{-2}, results in a first mode ENR transition value of 5 dB.

6

7
Figure 6 ENR transition values where processing with multiple modes become unbeneficial.

1   5.   EXPERIMENTAL APPLICATION

2   5.1   Methods

3   Figure 1 illustrated the experimental setup. The damage source is a steel rectangular (12.7 x 9.5 mm)

4   block with a mass of 13.2 grams. A Gaussian-windowed actuation signal at center frequency of 150 kHz

5   is induced by the 12.7 mm piezoelectric disc, and the scattered wave field sensed by a scanning laser

6   Doppler vibrometer (LDV) configured to sample a 7x7 array geometry with inter-element array scan

7   spacing of 6.35 mm. The laser vibrometer is configured in hardware with a low pass filter at a cutoff

8   frequency of 250 kHz and is sampled at a frequency of 1.25 MHz. The actuation frequency of 150 kHz is

9   selected as the largest actuation frequency that safely avoids spatial aliasing of the A_0 mode (Figure 4)

10   and as a frequency that experimentally resulted in a high signal to noise ratio of received waves at the

11   array. Retro-reflective tape is bonded to the plate over the array scan area to increase signal-to-noise ratio.

12   A LDV is used instead of fixed piezoelectric transducers since it allows for modification of array size and

13   geometry through software and additionally samples the wave field non-intrusively The use of the LDV

14   array also explains the chosen active sensing configuration where a single off array actuator interrogates

15   the plate and the LDV array senses since the LDV is incapable of actuation. The placement of the off

16   array actuator was chosen for experimental convenience such that any damage scattered signal would

17   arrive at the array with high a signal to noise ratio.

18   Collected array data was band-passed filtered between 100 and 200 KHz and spatially windowed

19   with a two dimensional Kaiser window function with window parameter $\beta = 2.5$[20,21]. One thousand

20   measurements were collected from no-damage (baseline) and damage states. Optimal minimum mean

21   square error baseline subtraction was employed resulting in 1000 measurements for the H_0 and H_1

22   hypotheses [22]. To aid in the comparison of the proposed detectors through ROC curves, measurements

23   form the H_0 hypothesis were randomly selected with replacement and added to both the H_0 and H_1

24   hypothesis. This was due to the large amount of backscatter from bonded mass which resulted in perfect

1   detection performance. Additionally, any scattering located within 50 mm of the plate edge was ignored.

2    $L = 48 \times 360$ range-bearing combinations were used for each detector for an average inspection area of

3   approximately $87 \, \text{mm}^2 / (\text{range-bearing bin})$.

4   5.2   Results

5   The detectors from Equations (20) and (21) are implemented for the signal models Equations (4)-

6   (6): 1) $S_0^{\{150\}}$, 2) $A_0^{\{150\}}$, 3) $S_0^{\{150\}} + A_0^{\{150\}}$ and 4) $A_0^{\{135\}} + A_0^{\{150\}}$. Here the excitation for 135 kHz is

7   obtained not from a separate excitation frequency but rather from using the original excitaiton signal at

8   150 kHz. This is possible by taking advantage of the excitation signal's finite bandwidth and the high

9   signal to noise ratio associted at 150 kHz excitaion. The performance of each detector is compared via

10   receiver operating curves [2], Figure 7, where each point on a curve corresponds to a value pair of $\left(P_{FA}, P_D \right)$

11   for a given threshold value γ. Experimentally, this is accomplished with a sliding threshold value, where

12   at a given threshold, the output of each detector is determined under H_0 and H_1 hypothesis. The number

13   of detector output values that exceed the threshold under each hypothesis are counted, and then the

14   probability of detection and false alarm estimated by dividing the count value by the number of

15   observations.
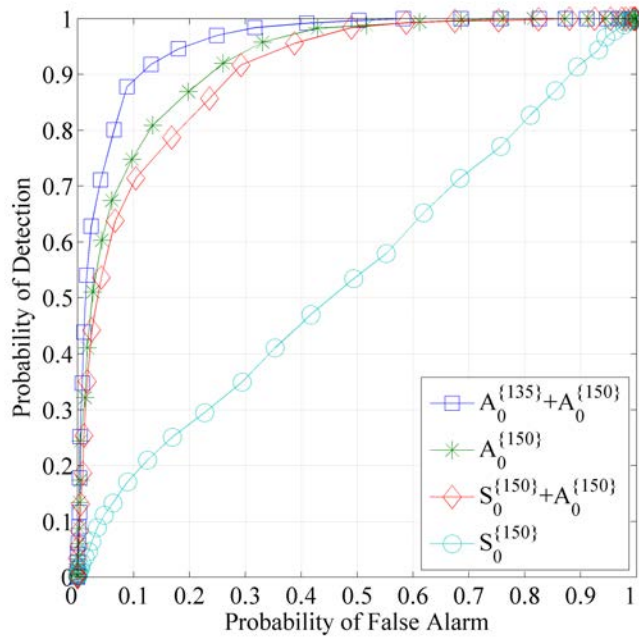
Figure 7 Receiver operator curves single and multimode detectors at 135 and 150 kHz.

Localization of damage for the detectors is shown as a histogram of the distance between the estimated and true location damage location (Figure 8).
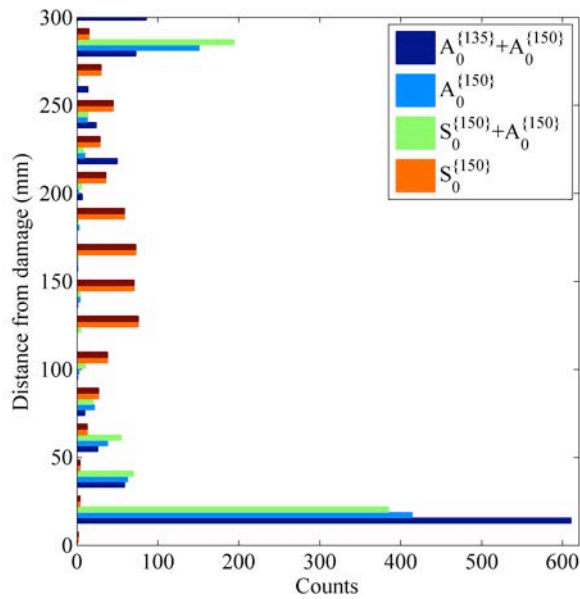

Figure 8 Histogram of distance (meters) between actual damage location and estimated multimode location.

6. DISCUSSION

1   The multi-frequency $A_0^{\{135\}} + A_0^{\{150\}}$ detector has the best performance, followed by the single

2   mode $A_0^{\{150\}}$ detector, then the multi-mode $S_0^{\{150\}} + A_0^{\{150\}}$ and finally the $S_0^{\{150\}}$ detector. Processing with

3   both the A_0 and S_0 modes results in a decrease in detection performance compared to processing with just

4   the A_0 mode. This is explained by assuming that backscatter power from damage is proportional to the

5   power from boundary reflections. Figure 9 and Figure 10 are backscattered power from the plate edges

6   for a non-baseline subtracted measurement, where the scales in dB are normalized to the maximum power

7   in the A_0 image map. The backscattered scattered power from the S_0 mode is approximately -12 dB lower

8   than the A_0 mode power; from the theoretical predictions of Figure 6, processing with a second mode

9   (S_0) power below -3.5 dB results in a decrease in detection performance. Similarly, the backscattered

10   power from the A_0 mode at 135 kHz is identical in shape to that of Figure 9 except that the normalized

11   power is only -2 dB below that of 150 kHz, resulting in an increase in detection performance when

12   processing with both frequencies.
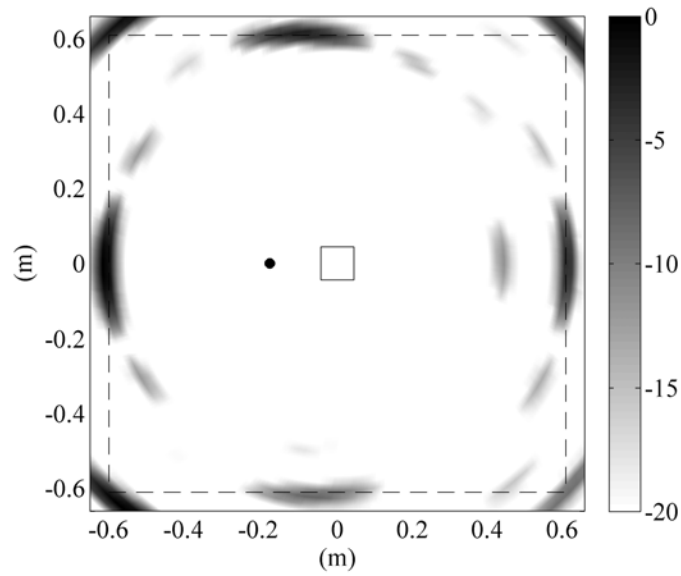
Figure 9 A_0 mode normalized back-scattered power (dB) from plate boundaries (dashed line). Scale is normalized to the maximum power value in the image map.
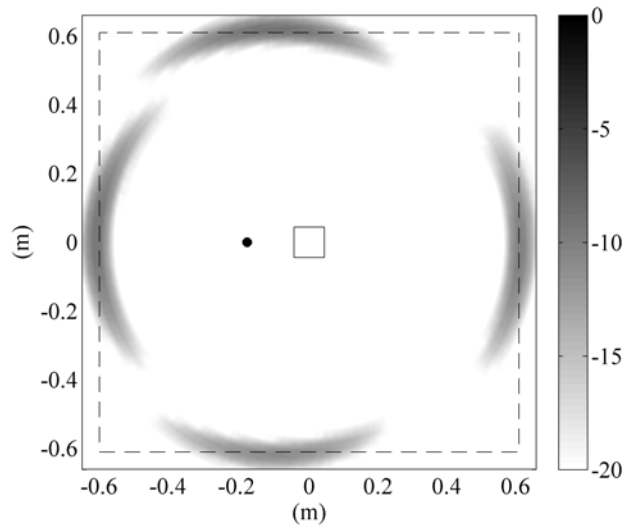
Figure 10 S_0 mode normalized back-scattered power (dB) from plate boundaries (dashed line). Scale is normalized to the maximum power value from the similar A_0 map of Figure 9.

1   The $A_0^{\{135\}} + A_0^{\{150\}}$ detector localization is superior to that of all detectors. The localization

2   accuracy of all detectors making use of the A_0 mode are bimodal with a peak occurring at a distance of 10

3   mm due to scatting from damage and a second peak at 300 mm due to secondary reflections. The image

4   map output of the $A_0^{\{135\}} + A_0^{\{150\}}$ detector for a single measurement case, Figure 11, helps to explain this.

5   The detector output and estimated damage location occurs at the point with the maximum intensity in the

6   image map, indicated with a white star. The known damage location is indicated with a white circle. The

7   dotted line is the image area boundary, located 50 mm from the true plate edge. In addition to the peak

8   occurring at the true damage location, several other peaks occur near the image area boundary. These

9   peaks are due to secondary reflections resulting from forward scattering and coherent residual scattering

10   from non-ideal baseline subtraction. Thus the peak at 300 mm results from the secondary boundary

11   reflections having a larger value than the direct scattering from damage.
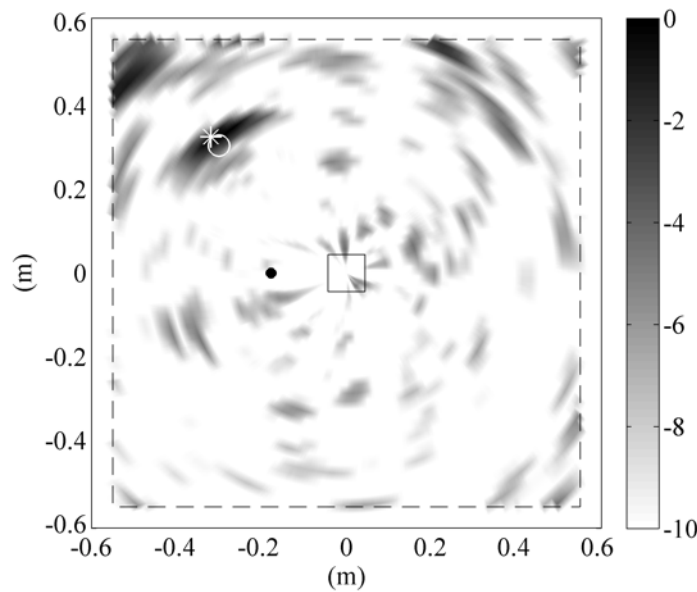
12

13   Figure 11 Multi-frequency, $A_0^{\{135\}} + A_0^{\{150\}}$, detector image map. The detector output and estimated damage location is the max
14   of image map, white star. The known damage location is at the center of the white circle.

1 7. CONCLUSION

2   A general active sensing signal model consisting of multiple plane waves scattered from a single

3 damage source and received by an array of transducers was assumed, allowing for modeling of many

4 UGWSHM damage cases ranging from single-mode scattering to mode-converted scattering to scattering

5 from multiple actuation frequencies. Amplitude and absolute phase of the scattered wave were assumed

6 unknown along with the location of the damage, while frequency, group velocity and phase velocity were

7 assumed known. Four cases of the general signal model were studied: (1) direct backscattering from the

8 A_0 mode (2) direct backscattering from the S_0 mode, (3) direct backscattering from both the A_0 and the

9 S_0 modes, and (4) direct backscattering from the A_0 mode at two different frequencies. Detectors were

10 derived for each model using a generalized likelihood ratio approach to decide between the null

11 hypothesis of damage not present and an alternative hypothesis of damage present. The resulting detectors

12 consisted of a phased array beamformer and a periodogram evaluated at a known frequency. Theoretical

13 detection performance for processing with each detector was derived and related to the energy to noise

14 ratio of a scattered mode as a metric of determining when processing with multiple modes provides better

15 performance than processing with a single mode. The detectors were studied experimentally for the

16 simulated damage case of a mass glued to the surface of an aluminum plate and compared through

17 experimental receiver operator curves and histograms of damage location.

18   Detectors containing the A_0 mode provided superior detection and localization performance compared

19 to the single S_0 mode model, attributed to the large amount of scattered energy from the A_0 modes and

20 small amount from the S_0 mode. Similarly, inclusion of the S_0 mode resulted in decreased performance

21 compared to processing with just a single A_0 mode. The $A_0^{\{135\}} + A_0^{\{150\}}$ detector resulted in the best

22 detection and localization performance of all detectors. The ability for superior detection performance of

23 a given mode type and or combination will be dependent upon the specific experimental situation such as

24 actuator and sensor type as well as the nature of the scattering induced by the damage.

Since a signal model is assumed, any deviations from the assumed model result in decreased performance. The major limitations of the assumed model and detectors are: (1) Assuming only a single scattering source limits the resulting detectors to structures where direct scattering from damage is the largest scattering source. If secondary scattering sources are larger than direct damage scatter, then boundaries cannot be imaged. (2) A Gaussian noise assumption made during the detector derivation is dependent upon an ideal baseline subtraction, which results in an uncorrelated signal except for the damage-scattered signal, and non-ideal subtraction may result in coherent noise, which would degrade detector performance. (3) Frequency, phase velocity and group velocity, are assumed known and if unknown, they must be estimated through a separate model, experimental testing, or other evidence.

Future work will focus on modeling the correlation associated with the multipath environment of UGWSHM structures, extending the assumed model to allow for non-baseline subtracted signals. Such an approach would include the modeling of interference sources from boundaries, particularly suited to hot spot monitoring where damage occurs in a specific location with known boundary reflections. Additionally, incorporating the interaction of a given guided wave with a specific damage type, such as relative scattered amplitudes and scattering profiles, into an the assumed model should further enhance detection, allowing for a more robust implementation.

8.   ACKNOWLEGEMENTS

9.   REFERENCES

1. Alleyne DN, Cawley P. The interaction of Lamb waves with defects. IEEE Transactions on Ultrasonics, Ferroelectrics and Frequency Control. 1992 May;39(3):381–97.

2. Kay SM. Fundamentals of Statistical Signal Processing Detection Theory. Prentice Hall Publishers; 1998.

3. Farrar CR, Worden K. An introduction to structural health monitoring. Philosophical Transactions of the Royal Society A: Mathematical, Physical and Engineering Sciences. 2007;365(1851):303–15.

4. Clarke T, Cawley P, Wilcox PD, Croxford AJ. Evaluation of the damage detection capability of a sparse-array guided-wave SHM system applied to a complex structure under varying thermal conditions. Ultrasonics, Ferroelectrics and Frequency Control, IEEE Transactions on. 2009 Dec;56(12):2666 –2678.

5. Michaels JE. Detection, localization and characterization of damage in plates with an in situ array of spatially distributed ultrasonic sensors. Smart Materials and Structures. 2008 Jun 1;17(3):035035.

6. Zhao X, Gao H, Zhang G, Ayhan B, Yan F, Kwan C, et al. Active health monitoring of an aircraft wing with embedded piezoelectric sensor/actuator network: I. Defect detection, localization and growth monitoring. Smart Materials and Structures. 2007 Aug 1;16(4):1208–17.

7. Ihn J-B, Chang F-K. Pitch-Catch Active Sensing Methods in Structural Health Monitoring for Aircraft Structures. Structural Health Monitoring. 2008 Mar 1;7(1):5–19.

8. Sundararaman S, Adams DE, Rigas EJ. Structural Damage Identification in Homogeneous and Heterogeneous Structures Using Beamforming. Structural Health Monitoring. 2005 Jun 1;4(2):171–90.

9. Giurgiutiu V, Bao J. Embedded-Ultrasonics Structural Radar for In Situ Structural Health Monitoring of Thin-Wall Structures. Structural Health Monitoring. 2004 Jun 1;3(2):121–40.

10. Flynn EB, Todd MD, Croxford AJ, Drinkwater BW, Wilcox PD. Enhanced detection through low-order stochastic modeling for guided-wave structural health monitoring. Structural Health Monitoring. 2011 Aug 9;11(2):149–60.

11. Haynes C, Todd MD, Flynn E, Croxford A. Statistically-based damage detection in geometrically-complex structures using ultrasonic interrogation. Structural Health Monitoring [Internet]. 2012 Dec 21 [cited 2013 Jan 14]; Available from: http://shm.sagepub.com/content/early/2012/12/20/1475921712466756

12. Giurgiutiu V. Tuned Lamb Wave Excitation and Detection with Piezoelectric Wafer Active Sensors for Structural Health Monitoring. Journal of Intelligent Material Systems and Structures. 2005;16(4):291–305.

13. Don H. Johnson, Dan E. Dudgeon. Array Signal Processing. 1st ed. Upper Saddle River, New Jersey: Prentice Hall Publishers;

14. Konstantinidis G, Drinkwater BW, Wilcox PD. The temperature stability of guided wave structural health monitoring systems. Smart Mater. Struct. 2006 Aug 1;15(4):967.

15. Cho Y, Hongerholt DD, Rose JL. Lamb wave scattering analysis for reflector characterization. IEEE Transactions on Ultrasonics, Ferroelectrics and Frequency Control. 1997;44(1):44–52.

16. Croxford AJ, Moll J, Wilcox PD, Michaels JE. Efficient temperature compensation strategies for guided wave structural health monitoring. Ultrasonics. 2010 Apr;50(4–5):517–28.

17. Flynn EB, Todd MD, Wilcox PD, Drinkwater BW, Croxford AJ. Maximum-likelihood estimation of damage location in guided-wave structural health monitoring. Proc. R. Soc. A. 2011 Sep 8;467(2133):2575–96.

18. Kay SM. Fundamentals of Statistical Signal Procesing Estimation Theory. Upper Saddle River, New Jersey: Prentice Hall Publishers; 1993.

19. Harris FJ. On the use of windows for harmonic analysis with the discrete Fourier transform. Proceedings of the IEEE. 1978 Jan;66(1):51 – 83.

20. Oppenheim AV, Schafer RW. Discrete Time Signal Processing. Oppenheim AV, editor. Prentice Hall Publishers; 1998.

21. Van Trees HL. Optimum Array Processing. New York: John Wiley and Sons; 2002.

22. Lu Y, Michaels JE. A methodology for structural health monitoring with diffuse ultrasonic waves in the presence of temperature variations. Ultrasonics. 2005 Oct;43(9):717–31.